FoCUS: Fourier-Based Coded Ultrasound

Almog Lahav, Tanya Chernyakova, *Student Member, IEEE*, and Yonina C. Eldar, *Fellow, IEEE*

***Abstract*— Modern imaging systems typically use single-carrier short pulses for transducer excitation. Coded signals together with pulse compression are successfully used in radar and communication to increase the amount of transmitted energy. Previous research verified significant improvement in signal-to-noise ratio (SNR) and imaging depth for ultrasound imaging with coded signals. Since pulse compression needs to be applied at each transducer element, the implementation of coded excitation (CE) in array imaging is computationally complex. Applying pulse compression on the beamformer output reduces the computational load but degrades both the axial and lateral point spread function, compromising image quality. In this paper, we present an approach for efficient implementation of pulse compression by integrating it into frequency domain beamforming. This method leads to significant reduction in the amount of computations without affecting axial resolution. The lateral resolution is dictated by the factor of savings in computational load. We verify the performance of our method on a Verasonics imaging system and compare the resulting images to time-domain processing. The computational savings are evaluated for a minimal sampling rate of four times the central frequency. We show that from 4- to 33-fold reduction is achieved as a function of the resulting lateral resolution, with no degradation of axial resolution. For an imaging system operating at a higher sampling rate, e.g., 10 times the central frequency, the savings can be as high as 77-fold. The efficient implementation makes CE a feasible approach in array imaging with the potential to enhance SNR as well as improve imaging depth and frame rate.**

***Index Terms*— Array processing, beamforming, coded excitation, ultrasound.**

I. Introduction

ULTRASOUND is a radiation free imaging modality with numerous applications. In standard ultrasound systems an array of transducer elements transmits a short single-carrier Gaussian pulse. During its propagation echoes are scattered by acoustic impedance perturbations in the tissue, and received by the array elements. These echoes are essentially a stream of replicas of the transmitted pulse implying that the axial resolution is defined by the pulse duration. The data, collected by the transducers, is sampled and digitally integrated in a way referred to as beamforming, yielding a signal steered in a predefined direction and optimally focused at each depth. Such a beamformed signal, referred to as a beam, forms a line in the image.

While the resolution is defined by the pulse duration, the resulting signal-to-noise ratio (SNR) and imaging depth are proportional to the amount of transmitted energy. One way to increase the energy is to transmit a longer pulse at the cost of resolution. Increasing the energy while retaining the same pulse duration, requires higher peak intensity levels, which can potentially damage the tissue and are thus limited by the Food and Drug Administration regulations. More elaborate coded signals are used in radar and communication to overcome the above tradeoff between the transmitted energy and resolution [1].

When coded signals are used for excitation, pulse compression is performed on the detected signal by applying a matched filter (MF) defined by the transmitted pulse shape. As a result, the received stream of pulses is converted to a stream of pulse's autocorrelations. The width of the pulse's autocorrelation is on the order of the inverse bandwidth [2], implying that the resolution is now defined only by the available system bandwidth and is independent of the pulse duration. Therefore, a longer pulse can be used to transmit more energy without degrading axial resolution. In coded ultrasound imaging phase-modulated signals are of interest since amplitude modulation is suboptimal in terms of energy.

Extensive studies show that, despite the frequency dependent attenuation characterizing biological tissues and the differences between the detection and imaging nature of radar and ultrasound, coded signals can be successfully used in medical imaging [3], [4]. Experimental results reported in [5] show improvement of 15–20 dB in SNR as well as 30–40 mm improvement in penetration depth. Due to these superior properties, coded excitation (CE) was successfully applied in numerous ultrasound modalities including B-mode [6], [7], flow [8]–[11], strain imaging [12], [13], and contrast enhanced imaging [14].

Increased penetration and SNR are crucial for applications where the amount of transmitted energy is inherently reduced, e.g., synthetic aperture and plane-wave imaging [15]–[17]. The feasibility of CE in plane-wave-based shear wave motion detection was recently studied, showing substantial performance improvement [17]. Beyond the improvement in imaging depth, high SNR enables utilization of higher frequencies and consequently better image resolution [18]. It has also been shown that CE can be used to increase frame rate by simultaneous transmission of several coded orthogonal beams [19].

A. Challenges and Existing Solutions

Despite the proven advantages of coded imaging its application in commercial medical systems is still very limited. One of the main challenges of CE in medical ultrasound is its application to imaging with an array of transducer

Manuscript received August 30, 2017; accepted September 25, 2017. Date of publication October 6, 2017; date of current version December 1, 2017. *(Almog Lahav and Tanya Chernyakova contributed equally to this work.) (Corresponding author: Tanya Chernyakova.)*

The authors are with the Department of Electrical Engineering, Technion–Israel Institute of Technology, Haifa 3200003, Israel (e-mail: ctanya@campus.technion.ac.il).

Digital Object Identifier 10.1109/TUFFC.2017.2760359

elements due to the computational complexity of the required processing [3], [20]–[22]. Regardless of the type of transmitted signal, sampling rates required to perform high resolution digital beamforming are typically significantly higher than the Nyquist rate of the signal. Rates up to 4–10 times the central frequency of the transmitted pulse are used in order to eliminate artifacts caused by digital implementation of beamforming in time [23]. Taking into account the number of transducer elements, the amount of sampled data that needs to be transferred to the processing unit and digitally processed in real time is typically on the order of 10^8 samples per frame.

The pulse compression step, required in coded imaging, further increases the computational load. In particular, implementation of CE in array imaging requires an MF for every transducer element. Most reported experimental studies use either a single transducer element [4], [13], [14] or an array of elements with one MF applied on the beamformed output [3], [5]. Despite the advantage of a single MF application on the beamformed data from a computational perspective, this approach degrades the performance of pulse compression [3]. The process of beamforming is comprised of averaging the received signals after their alignment with appropriate delays. To obtain dynamic focusing the applied delays are nonlinear and time dependent and, thus, distort the phases of the coded signals. Due to this distortion the range (axial) sidelobe level and the main lobe width of the MF output are degraded, leading to decreased contrast and resolution, which are highly prominent at low imaging depths [20]. This is especially problematic for plane-wave-based imaging where the depth of interest is typically up to 5 cm and CE is used to increase the amount of transmitted energy.

One way to minimize this effect is to limit the duration of the transmitted pulse [5]. However, this obviously reduces the amount of transmitted energy and, thus, goes against the main motivation behind the usage of coded signals. Another approach is based on the observation that the degradation in compression performance due to dynamic beamforming depends on the transmit focus depth [20]. A possible solution, therefore, is to divide an image into several depth zones and adjust the code length according to the depth in order to reduce compression error. However, this increases the number of transmissions in accordance to the number of focal zones, which in turn increases acquisition time.

B. Contributions

Here we propose an approach that achieves perfect pulse compression, while keeping the computational complexity low. Our method is based on incorporating pulse compression into frequency domain beamforming (FDBF) developed recently for medical ultrasound [24]–[26]. This allows to use an MF in each transducer element at a low cost.

The concept of beamforming in frequency was first addressed back in the sixties for sonar arrays operating in the far field. However, translating these ideas to ultrasound imaging is much more involved due to the near-field operation, requiring nonlinear beamforming. To the best of our knowledge, it was first addressed in [24] and [25], where it was shown that in the frequency domain the Fourier components of the beamformed signal can be computed as a weighted average of those of the individual detected signals. Since the beam is obtained directly in frequency, its Fourier components are computed only within its effective bandwidth. This is performed using generalized low-rate samples of the received signals, implying sampling and processing at the effective Nyquist rate which is defined with respect to the signal's effective bandpass bandwidth [27].

According to the convolution theorem, pulse compression applied at each transducer element through an MF is equivalent to multiplication in the frequency domain. In this paper, we show that it can be applied by appropriate modification of the weights required for FDBF. As a result, not only is beamforming performed in frequency at a low rate, but it also includes match filtering each individual channel without any additional computational load. The proposed method, performing both beamforming and pulse compression in frequency, is referred to as FoCUS: Fourier-based Coded UltraSound.

The performance of our method is verified on a Verasonics ultrasound system and compared to time-domain processing in terms of axial and lateral resolution. We evaluate the computational load for typical imaging setups and show that it can be reduced by 4- to 77-fold compared to the time-domain implementation, depending on the oversampling factor and the required lateral resolution. The axial resolution obtained by FoCUS remains optimal regardless of the reduction in complexity. This efficient implementation may pave the way for CE to become practical in array imaging.

The rest of this paper is organized as follows. Section II reviews basics of CE applied to medical imaging. In Section III, we discuss the requirements and challenges of CE in the context of array imaging. We then introduce our approach based on FDBF in Section IV. Experimental results and the performance of FoCUS in terms of image quality and computational complexity are presented in Section V.

II. Coded Excitation in Medical Ultrasound

In CE, a modulated signal is used for transducer excitation

$$s(t) = a(t)\cos(2\pi f_0 t + \psi(t)), \quad 0 \le t \le T_p \tag{1}$$

where $\psi(t)$ and $a(t)$ are phase and amplitude modulation functions, respectively, f_0 is the transducer central frequency and T_p is the signal duration. Assuming a nonattenuating medium and disregarding other nonlinear effects, for L scatterers along the propagation path, the reflected signal, $\varphi(t)$, detected by an individual transducer element is given by

$$\varphi(t) = \sum_{l=1}^{L} \alpha_l s(t - t_l) \tag{2}$$

where $\{\alpha_l\}_{l=1}^{L}$ and $\{t_l\}_{l=1}^{L}$ are amplitudes and delays defined, respectively, by the scatterer's reflectivity and location.

Pulse compression is performed on the detected signal, $\varphi(t)$, by applying an MF, $h(t) = s^*(-t)$. The output is then a

combination of autocorrelations of the transmitted pulse [28]

$$\varphi^{\mathrm{CE}}(t) = \varphi(t) * s^*(-t) = \sum_{l=1}^{L} \alpha_l R_{ss}(t - t_l) \tag{3}$$

where the autocorrelation is given by

$$R_{ss}(t) = \int_{-\infty}^{\infty} s(\tau) s^*(\tau - t) d\tau. \tag{4}$$

The half-power width of the main lobe of the autocorrelation, which determines the range resolution, is approximately equal to the inverse bandwidth B^{-1} [2] of the transmitted pulse. As a result, in contrast to conventional imaging, the pulse time duration, T_p, can be increased and more energy transmitted without degrading range resolution. The resulting gain in SNR of the MF processing is approximately equal to the time-bandwidth product $D = T_p B$ [29].

The above analysis assumes the detected signal is comprised of the exact replicas of the transmitted pulse. In practice, when acoustic waves propagate in biological tissues, high frequencies undergo stronger attenuation due to the medium properties. For a signal with a Gaussian spectrum a common way to model this effect is to assume that it does not distort the complex envelope of the reflected signal and only downshifts its central frequency [30]. Even though this model is less accurate for a non-Gaussian spectrum [22] with high central frequency and bandwidth, it provides meaningful insight into the performance of pulse compression in attenuating media [28] and, thus, is used in our discussion below. Under this approximation, the pulse reflected from the lth scatterer is given by

$$s(t - t_l, f_l) = a(t - t_l) \cos(2\pi (f_0 - f_l)(t - t_l) + \psi(t - t_l)). \tag{5}$$

As a result, the MF output depends on the central frequency shift, f_l, and is given by

$$A(t - t_l, f_l) = \int_{-\infty}^{\infty} s(\tau - t_l, f_l) s^*(\tau - t) d\tau. \tag{6}$$

The function $A(t, f)$ is referred to as the ambiguity function. Similar to (3), for L scatterers, the output of the MF is a stream of cross sections of ambiguity functions

$$\varphi^{\mathrm{CE}}(t) = \varphi(t) * s^*(-t) = \sum_{l=1}^{L} \alpha_l A(t - t_l, f_l). \tag{7}$$

In ultrasound imaging the frequency shifts do not carry valuable information and thus do not need to be determined explicitly. However, the width of the main lobe of the ambiguity function needs to be small for all values of f_l to ensure good axial resolution for all frequency shifts. The ambiguity function of linear frequency modulation (FM) has this property and therefore FM is a good choice for CE ultrasound imaging.

The expression for a linear FM signal is

$$s(t) = a(t) \cos\left(2\pi \left((f_0 - B/2)t + \frac{B}{2T_p} t^2\right)\right), \quad 0 \le t \le T_p. \tag{8}$$

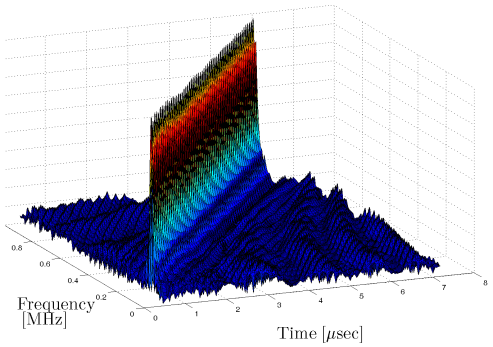

Fig. 1. Ambiguity function of linear FM with time-bandwidth product of $D = 70$.

When no tapering is presented, i.e., $a(t)$ in (8) is a rectangular window, the frequency spectrum of the linear FM complex envelope is rectangular, so that the envelope of the MF output is approximately a sinc function [31]. The ambiguity function of a linear FM signal is shown in Fig. 1. One can recognize the shape of a sinc in the cross sections parallel to the frequency axis. Note that these cross sections preserve the same main lobe width for every frequency shift. Theoretically, this is true when there is no distortion of the spectrum except the frequency shift. The results in [4] show that the main lobe width indeed remains constant for imaging with linear FM in attenuating media.

A significant improvement in penetration depth and contrast with linear FM excitation are reported in [4]. However, these are obtained with a single-element transducer, while imaging systems today use an array of transducer elements. The implication of array processing on pulse compression is discussed next.

III. Use of Coded Excitation in Array Imaging

A. Conventional Array Imaging

Most commercial imaging systems today use multiple transducer elements to transmit and receive acoustic pulses, enabling spatial selectivity of signal transmission or reception. The selectivity is obtained by beamforming which is comprised of applying dynamically changing delays on the signals received at each one of the transducer elements prior to averaging [32]. Time-varying delays allow dynamic shift of the reception beam's focal point, optimizing angular resolution. Averaging of the delayed signals in turn enhances the SNR of the resulting beamformed signal, which is used to form a line in an image.

Consider an array of M elements, illustrated in Fig. 2. Denote by m_0 the reference element, by δ_m its distance to the mth element, and by c the speed of sound. The image cycle begins at $t = 0$, when an energy pulse starts to propagate in the direction θ and at time $t \ge 0$ reaches a potential point reflector located at $(x, z) = (ct \sin\theta, ct \cos\theta)$. Denote by $\varphi_m(t)$ the signal received by the mth element and by $\hat{\tau}_m(t; \theta)$ the time of arrival. It is readily seen that

$$\hat{\tau}_m(t; \theta) = t + \frac{d_m(t; \theta)}{c} \tag{9}$$

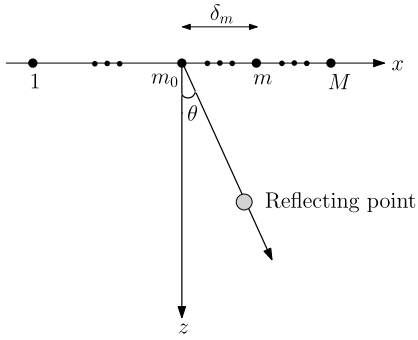

Fig. 2. M receivers aligned along the x-axis. An acoustic pulse is transmitted in a direction θ.

where $d_m(t;\theta) = \left((ct\cos\theta)^2 + (\delta_m - ct\sin\theta)^2\right)^{1/2}$ is the distance traveled by the reflection. Beamforming involves averaging the signals received by multiple receivers while compensating for the differences in arrival time.

Since $\delta_{m_0} = 0$, the arrival time at m_0 is $\hat{\tau}_{m_0}(t;\theta) = 2t$. Applying an appropriate delay to $\varphi_m(t)$, such that the resulting signal $\hat{\varphi}_m(t;\theta)$ satisfies $\hat{\varphi}_m(2t;\theta) = \varphi_m(\hat{\tau}_m(t;\theta))$, we align the reflection received by the mth receiver with the one received at m_0. Denoting $\tau_m(t;\theta) = \hat{\tau}_m(t/2;\theta)$ and using (9), the following aligned signal is obtained:

$$\hat{\varphi}_m(t;\theta) = \varphi_m(\tau_m(t;\theta))$$
$$\tau_m(t;\theta) = \frac{1}{2}\left(t + \sqrt{t^2 - 4(\delta_m/c)t\sin\theta + 4(\delta_m/c)^2}\right). \quad (10)$$

The beamformed signal may now be derived by averaging the aligned signals

$$\Phi(t;\theta) = \frac{1}{M}\sum_{m=1}^{M}\hat{\varphi}_m(t;\theta) = \frac{1}{M}\sum_{m=1}^{M}\varphi_m(\tau_m(t;\theta)). \quad (11)$$

Such a beam is optimally focused at each depth and hence exhibits improved angular localization and enhanced SNR. Although derived here over continuous time, the processing in (11) in practice is performed digitally.

Averaging of the aligned signals may also include dynamic apodization allowing to reduce the sidelobes of the lateral point spread function (PSF) at the expense of a wider main lobe. This is performed by multiplying each of the aligned signals by a time-dependent function $w_m(t)$. As shown in [33], dynamic apodization can be easily incorporated into frequency domain processing.

B. Matched Filtering and Beamforming

As explained in Section II, in the CE approach, pulse compression is achieved by applying an MF on the detected signal. Array imaging requires matched filtering of the detected signal at every transducer element prior to beamforming, as illustrated in Fig. 3. This implementation is referred to as beamforming precompression [20], since beamforming is applied after compression. Using (11) and substituting the MF impulse response $h(t) = s^*(-t)$, the beamformed signal is given by

$$\Phi_{\mathrm{CE}}(t;\theta) = \frac{1}{M}\sum_{m=1}^{M}\varphi_m^{\mathrm{CE}}(\tau_m(t;\theta))$$
$$\varphi_m^{\mathrm{CE}}(t) = \{\varphi_m * h\}(t). \quad (12)$$

The computational complexity in this implementation is vastly increased by filtering each detected signal, restricting the use of CE in array imaging.

A straightforward way to overcome the computational bottleneck is beamforming postcompression, i.e., performing beamforming on the uncompressed detected signals and applying the MF on the beamformer's output [20]. This requires only one MF leading to a reduction in the number of multiplies by a factor N where

$$N \approx (M-1)\left(\frac{3}{2}(N_s+N_h)\log(N_s+N_h) + N_s + N_h\right) \quad (13)$$

and M, N_s, and N_h are the number of elements, number of samples, and MF length, respectively. Further reduction in computational complexity can be obtained if the pulse compression is performed on baseband beamformed data as proposed in [21] and [22]. The computational savings achieved with this approach are discussed in detail in Section V-D.

The advantage of a single application of MF on the beamformed data is obvious from the computational perspective. However, with this approach the resulting beamformed signal is given by

$$\Phi_{\mathrm{CE_{post}}}(t;\theta) = \left\{\frac{1}{M}\sum_{m=1}^{M}\varphi_m(\tau_m(t;\theta))\right\} * h(t). \quad (14)$$

As can be seen in (10), the applied delay $\tau_m(t;\theta))$ is a nonlinear function of time and varies within the support of the coded pulse. Consequently, the detected signal is distorted and is no longer comprised of exact replicas of the transmitted pulse. Due to this distortion the impulse response of the MF is mismatched with the input signal leading to poor compression performance: sidelobe level and main lobe width are degraded decreasing resolution and contrast. These effects are especially prominent at low imaging depths in the near field, where the beamforming delays are the most significant. Experimental comparison of beamforming precompression and postcompression performances is performed in Section V-B. A detailed study of the effect of beamforming precompression and postcompression on image quality is presented in [5] and [20].

IV. Beamforming and Pulse Compression in the Frequency Domain

To obtain a computationally efficient method for matched filtering at each transducer element prior to beamforming, we propose integrating the MF into the FDBF framework.

As mentioned in Section I, beamforming in frequency was first considered in the context of sonar array processing [34], [35], where due to the far-field operation mode corresponds to averaging the signals after applying constant delays. This process can be transferred to the frequency

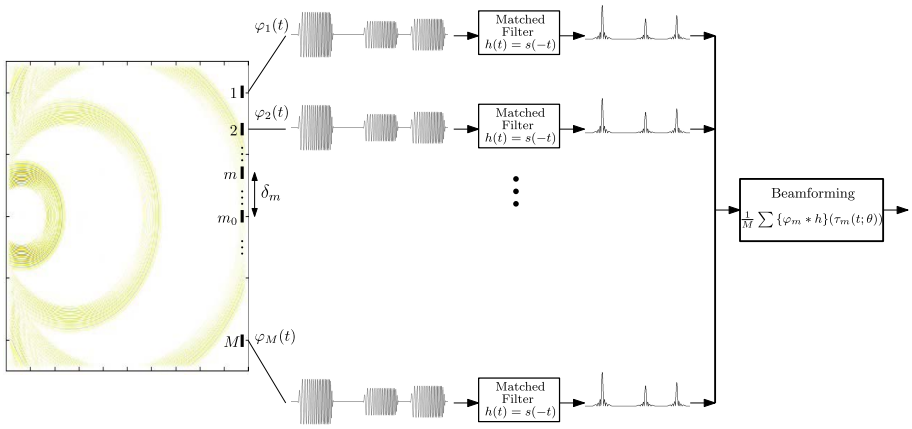

Fig. 3. On the left, echoes are reflected from three point scatterers in the medium. The received signal at each transducer element is composed of reflections of a linear FM waveform. Beamforming is applied on compressed signals, obtained at the output of the MF at each element.

domain in a straightforward manner through the well-known time shifting property of the Fourier transform. In the context of ultrasound imaging, due to the dynamic nature of beamforming which implies nonlinearity and time dependence of the required delays, the translation to frequency is much more involved. A frequency domain formulation of beamforming was introduced in [25] and [26] for 2-D imaging and 3-D imaging, respectively, leading to significant reduction in sampling and processing rates. We begin by reviewing the above framework based on [25] and then show how to incorporate pulse compression into it without increasing the computational cost.

A. Prior Art: Frequency Domain Beamforming

Ultrasound operates in extreme near field. Therefore, to obtain the far-field beampattern of the array allowing for spatial selectivity, dynamic focusing is required. The focal point is moved throughout the scan depth by applying time dependent delays $\tau_m(t;\theta)$ defined in (10). Despite the nonlinearity of the delays, the Fourier components of the beamformed signal can be computed as a weighted average of those of the individual detected signals [25].

To this end, denote the Fourier coefficients of $\Phi(t;\theta)$ with respect to the interval T, defined by the maximal scan depth, by

$$c[k] = \frac{1}{T}\int_0^T I_{[0,T_B(\theta))}(t)\Phi(t;\theta)e^{-i\frac{2\pi}{T}kt}dt \tag{15}$$

where $I_{[a,b)}$ is the indicator function equal to 1 when $a \le t < b$ and 0 otherwise and $T_B(\theta) = \min_{1\le m\le M}\tau_m^{-1}(T;\theta)$ [24]. Substituting (11) into (15) results in

$$c[k] = \frac{1}{M}\sum_{m=1}^{M}\hat{c}_m[k] \tag{16}$$

where

$$\begin{aligned}\hat{c}_m[k] &= \frac{1}{T}\int_0^T I_{[0,T_B(\theta))}(t)\varphi_m(\tau_m(t;\theta))e^{-i\frac{2\pi}{T}kt}dt \\ &= \frac{1}{T}\int_0^T \varphi_m(t)q_{k,m}(t;\theta)e^{-i\frac{2\pi}{T}kt}dt.\end{aligned} \tag{17}$$

The last equation stems from the variable substitution $x = \tau_m(t;\theta)$, required to obtain $c[k]$ as a function of nondelayed receive signals $\varphi_m(t)$. The delays are effectively applied through the so-called distortion function, $q_{k,m}(t;\theta)$, given by

$$\begin{aligned}q_{k,m}(t;\theta) = I_{[|\gamma_m|,\tau_m(T;\theta))}(t)\left(1+\frac{\gamma_m^2\cos^2\theta}{(t-\gamma_m\sin\theta)^2}\right) \\ \times\exp\left\{i\frac{2\pi}{T}k\frac{\gamma_m - t\sin\theta}{t-\gamma_m\sin\theta}\gamma_m\right\}\end{aligned} \tag{18}$$

with $\gamma_m = \delta_m/c$.

To derive a relationship between the Fourier coefficients of the beam and those of the received signals, we next replace $\varphi_m(t)$ by its Fourier coefficients $c_m[n]$ and rewrite (17) as

$$\begin{aligned}\hat{c}_m[k] &= \sum_n c_m[n]\frac{1}{T}\int_0^T q_{k,m}(t;\theta)e^{-i\frac{2\pi}{T}(k-n)t}dt \\ &= \sum_n c_m[k-n]Q_{k,m;\theta}[n].\end{aligned} \tag{19}$$

Here $Q_{k,m;\theta}[n]$, referred to as Q-coefficients, are the Fourier coefficients of the distortion function with respect to $[0,T)$. When substituted by its Fourier coefficients, the distortion function effectively transfers the beamforming delays defined in (10) to the frequency domain. The function $q_{k,m}(t;\theta)$ depends only on the array geometry and is independent of the received signals. Therefore, its Fourier coefficients can be computed off-line and used as a lookup table during the imaging cycle. According to Proposition 1 in [24], $\hat{c}_m[k]$ can be approximated sufficiently well with a finite number N_q of Q-coefficients

$$\hat{c}_m[k] \simeq \sum_{n=-N_1}^{N_2} c_m[k-n]Q_{k,m;\theta}[n] \tag{20}$$

where $N_q = N_2 - N_1 + 1$. The choice of N_q controls the approximation quality. As reported in [25] for $n < -N_1$ and $n > N_2$, the coefficients $\{Q_{k,m;\theta}[n]\}$ are several orders of magnitude lower than $Q_{k,m;\theta}[0]$ and therefore may be neglected, allowing for efficient implementation of beamforming in frequency. The choice of N_q and its effect on image quality are discussed in detail in Section V-C.

Finally, substitution of (20) into (16) yields the desired relationship between the Fourier coefficients of the beam and the individual signals

$$c[k] \simeq \frac{1}{M} \sum_{m=1}^{M} \sum_{n=-N_1}^{N_2} c_m[k-n] Q_{k,m;\theta}[n]. \tag{21}$$

Applying an inverse Fourier transform on $\{c[k]\}$ results in the beamformed signal in time. We note that there is no need for envelope detection since we directly compute the one-sided spectrum of the beamformed signal. We then proceed to standard image generation steps which include log-compression and interpolation.

B. Integrating Pulse Compression Into Frequency Domain Beamforming

To incorporate pulse compression into the FDBF framework we aim to express the Fourier coefficients of the signal $\Phi_{\mathrm{CE}}(t;\theta)$, obtained by beamforming the compressed signals, as a function of the Fourier coefficients of the individual detected signals. This will allow performing the compression by means of weighting in the frequency domain together with beamforming.

Applying the steps in Section IV-A on $\Phi_{\mathrm{CE}}(t;\theta)$, its Fourier coefficients are given by

$$\begin{aligned} c_{\mathrm{CE}}[k] &= \frac{1}{M} \sum_{m=1}^{M} \hat{c}_m^{\mathrm{CE}}[k] \\ \hat{c}_m^{\mathrm{CE}}[k] &= \frac{1}{T} \int_0^T \varphi_m^{\mathrm{CE}}(t) q_{k,m}(t;\theta) e^{-i\frac{2\pi}{T}kt} dt \end{aligned} \tag{22}$$

with $q_{k,m}(t;\theta)$ defined in (18). Next, we replace $\varphi_m^{\mathrm{CE}}(t)$ by its Fourier coefficients $c_m^{\mathrm{CE}}[n]$

$$\hat{c}_m^{\mathrm{CE}}[k] \simeq \sum_{n=-N_1}^{N_2} c_m^{\mathrm{CE}}[k-n] Q_{k,m;\theta}[n]. \tag{23}$$

According to (12) and the convolution theorem, $c_m^{\mathrm{CE}}[n]$ are equal to $c_m[n]h[n]$, where $c_m[n]$ and $h[n]$ are the Fourier coefficients of the signal $\varphi_m(t)$ and the MF, respectively. This allows us to rewrite (20) as

$$\begin{aligned} \hat{c}_m^{\mathrm{CE}}[k] &\simeq \sum_{n=-N_1}^{N_2} c_m[k-n] h[k-n] Q_{k,m;\theta}[n] \\ &= \sum_{n=-N_1}^{N_2} c_m[k-n] \tilde{Q}_{k,m;\theta}[n]. \end{aligned} \tag{24}$$

The decaying property of $\{Q_{k,m;\theta}[n]\}$ is retained after integration of the MF: numerical studies show that most of the energy of $\{\tilde{Q}_{k,m;\theta}[n]\}$ is concentrated around the dc component, irrespective of the choice of k, m and θ. We illustrate these decay properties in Fig. 4, where $\{\tilde{Q}_{k,m;\theta}[n]\}$ is plotted as a function of n for $k = 130$, $m = 14$, $\theta = 0.427$ [rad].

Obviously, incorporation of pulse compression does not affect computational complexity of FDBF, since it only requires to update the set of frequency weights which is performed off-line. Substitution of (24) into (22) yields a relationship between the Fourier coefficients of the beam and the individual detected signals

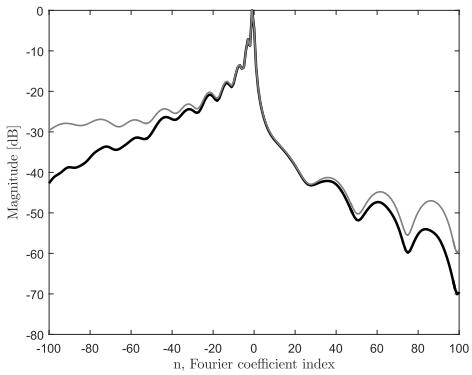

Fig. 4. Fourier coefficients $\tilde{Q}_{k,m;\theta}[n]$ and $Q_{k,m;\theta}[n]$ are characterized by a rapid decay. The black bold line is $\tilde{Q}_{k,m;\theta}[n]$ and the gray thin line is $Q_{k,m;\theta}[n]$. ($k = 130$, element number $m = 14$, angle $\theta = 0.427$[rad]).

$$c_{\mathrm{CE}}[k] \simeq \frac{1}{M} \sum_{m=1}^{M} \sum_{n=-N_1}^{N_2} c_m[k-n] \tilde{Q}_{k,m;\theta}[n]. \tag{25}$$

Applying an inverse Fourier transform on $\{c_{\mathrm{CE}}[k]\}$ results in a time-domain output equivalent to beamforming the detected compressed signals.

C. Processing at the Effective Nyquist Rate

We next consider the number of Fourier coefficients of the beamformed signal $\Phi_{\mathrm{CE}}(t;\theta)$ that need to be computed using (25) and explain how the Fourier coefficients of the individual detected signals, required for computation, are obtained. Denote by γ the set of Fourier coefficients of the MF output, $\varphi_m^{\mathrm{CE}}(t)$, that corresponds to its bandwidth, namely, the values of k for which $c_m^{\mathrm{CE}}[k]$ are nonzero (or larger than a threshold). Let G denote the cardinality of γ. According to (22) and (23), the bandwidth of the beamformed signal contains at most $K = G + N_q$ nonzero frequency components. In a typical imaging setup the value of G is on the order of hundreds, while N_q, defined by the decay properties of $\{Q_{k,m;\theta}[n]\}$, is typically on the order of tens. This implies that $K \approx G$, so that the bandwidth of the beam is approximately equal to the bandwidth of the MF output.

From (25), K Fourier coefficients of the beamformed signal are computed using at most $K + N_q$ Fourier coefficients of the individual detected signals. The latter can be obtained from $K + N_q$ point-wise samples of the detected signal filtered with an analog kernel $s^*(t)$. In ultrasound imaging with modulated pulses the transmitted signal has one main band of energy. Consequently, the analog filter takes on the form of a bandpass filter, leading to a simple low-rate sampling scheme [25].

The computational complexity of FoCUS and the achieved savings are discussed in detail in Section V-D.

V. Results

A. Experimental Setup

In order to examine the performance of the proposed method, we used real data acquired by Vantage 256,

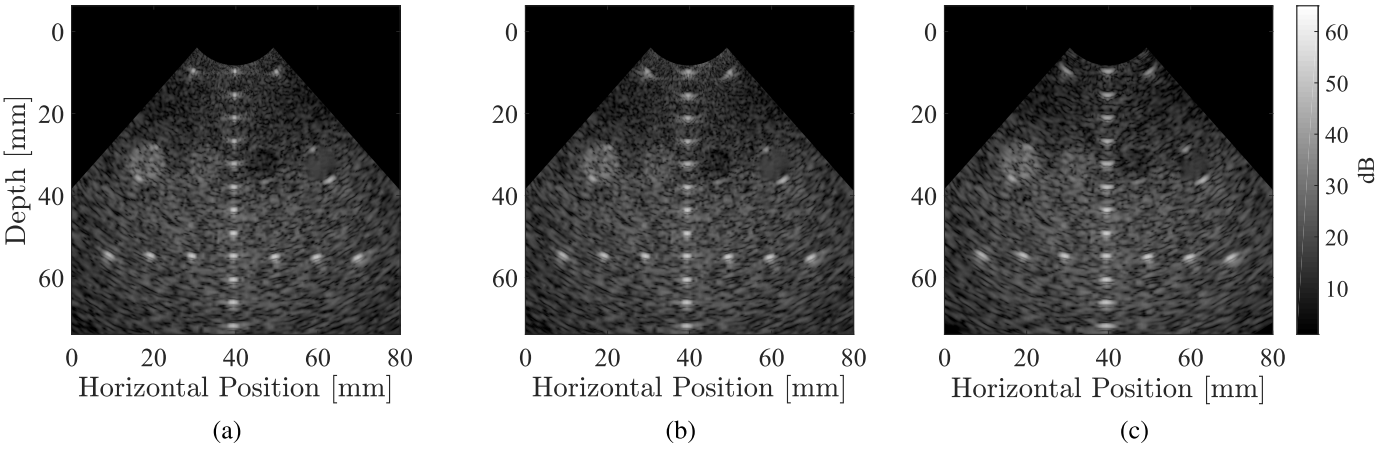

Fig. 5. Experimental results. Phantom scans obtained by (a) time domain beamforming precompression, (b) time domain beamforming postcompression, and (c) time domain beamforming postcompression with dynamic apodization.

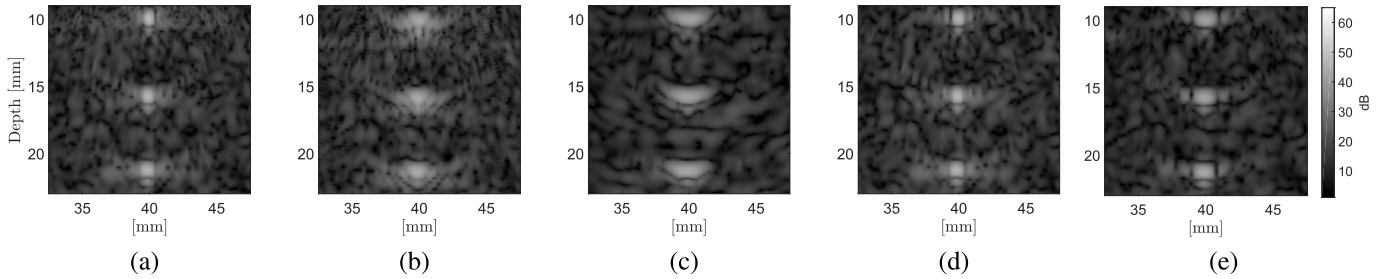

Fig. 6. Experimental results, zoomed-in view. Phantom scans obtained by (a) time domain beamforming precompression, (b) time domain beamforming postcompression, (c) time domain beamforming postcompression with dynamic apodization, (d) FDBF with $N_q = 29$, and (e) FDBF with $N_q = 9$.

an ultrasound system of Verasonics. A tissue mimicking phantom Gammex 404GSLE of 90-mm depth was scanned by a 64-element phased array transducer P4-2v with a frequency response centered at $f_c = 2.9$ MHz. All the elements were activated both on transmission and reception. During acquisition, each element transmitted a linear FM defined in (8) with length $T_p = 22.07$ μsec, central frequency $f_0 = 3$ MHz, and bandwidth $B = 2.72$ MHz, yielding a time-bandwidth product of $D = 60$. A Gaussian tapering window was used. No apodization was applied on transmission and reception. The raw data was processed using FoCUS defined in (25) for different approximation levels, namely, different number of Q-coefficients, N_q. The performance in axial and lateral dimensions for different values of N_q are compared to time domain beamforming precompression and postcompression. Savings in computational complexity for different values of N_q are discussed in Section V-D.

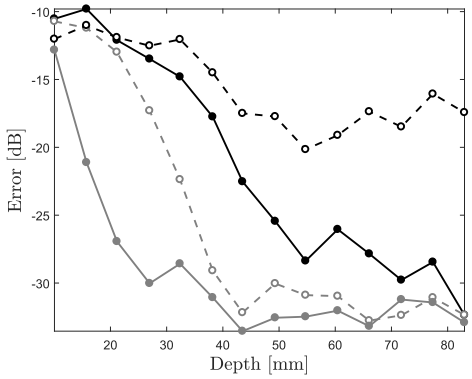

Fig. 7. Error between beamforming precompression and other methods as a function of depth. Black dashed and solid lines correspond to comparison to postcompression with and without dynamic apodization, respectively. Gray dashed and solid lines correspond to comparison to frequency processing with $N_q = 9$ and 29, respectively.

B. Beamforming Precompression and Postcompression Evaluations

We start with beamforming precompression and postcompression performances comparison. Images obtained by each method are presented in Fig. 5(a) and (b). Image quality degradation is most prominent at low depths. This can be seen in a zoomed-in view on the three first point reflectors shown in Fig. 6(a) and (b). As expected, with the increase of depth, the degradation decreases. To verify this quantitatively, we computed an error between the precompression and postcompression signals as a function of depth. Following the definition in [20], the error is given by:

$$\epsilon(z) = 10 \log_{10} \left(\frac{\sum_l \left(\Phi_{\text{pre}}(l,z) - \Phi_{\text{post}}(l,z) \right)^2}{\sum_l \left(\Phi_{\text{pre}}(l,z) \right)^2} \right). \quad (26)$$

Here $\Phi_{\text{pre}}(l,z)$ and $\Phi_{\text{post}}(l,z)$ stand for the envelope of the beamformed data at the location (l,z) for precompression and postcompression, respectively. The error as a function of depth is shown in Fig. 7 and is consistent with the results in [20].

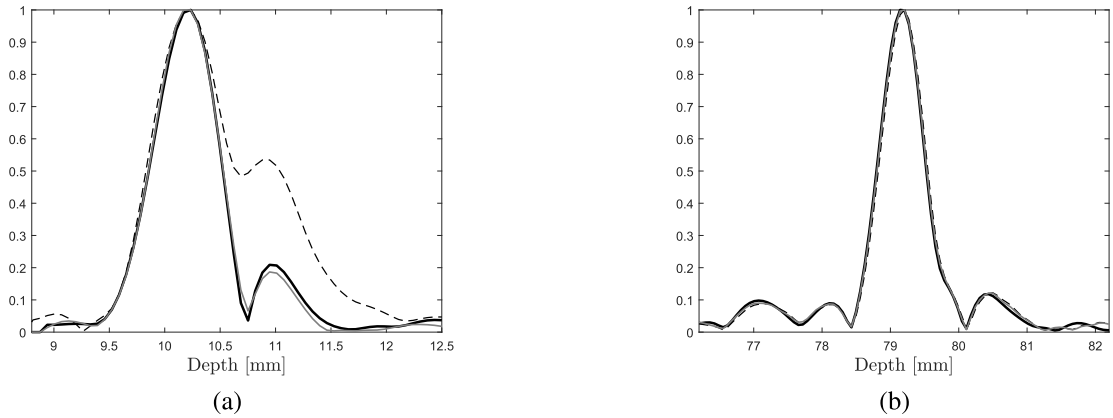

Fig. 8. Scan-lines of a point scatterer located at different depths. Frequency domain processing with $N_q = 9$ in black bold line, beamforming precompression in gray thin line, and beamforming postcompression in dashed line. (a) Scatterer located around 10 mm. (b) Scatterer located around 80 mm.

Fig. 8(a) and (b) shows scan-lines of a point scatterer located at 10 and 80 mm from the transducer, respectively. The chosen locations correspond to the minimal and the maximal imaging depth. As can be seen in Fig. 8(a), for 10-mm depth the main lobe of the resulting axial PSF is approximately 13% wider when beamforming is performed prior to pulse compression. In addition, the sidelobe is 9 dB higher. As expected, at the depth of 80-mm PSFs of precompression and postcompression are almost indistinguishable. We note that the error is relatively high up to 40 mm, which is a typical depth for plane-wave-based imaging including shear wave elastography of breast, carotid and thyroid [36].

The performance of beamforming postcompression at shallow depths can be improved by introducing dynamic apodization. In this case, the edge elements with highest values of the beamforming delays receive lower weights. This decreases their contribution to the beamformer output and consequently improves compression performance. The effect of dynamic apodization with a Hamming window and f-number equals to 2 on performance of beamforming postcompression is shown in Figs. 5(c) and 6(c). The corresponding error, presented in Fig. 7, shows that at lower depth there is indeed an improvement of approximately 1.3 dB. However, visual inspection of Figs. 5 and 6 shows that the even with dynamic apodization the performance of postcompression is reduced compared to precompression. In addition, as the depth increases, the error becomes larger compared to postcompression without dynamic apodization. Optimal performance for beamforming postcompression may be obtained by appropriately adjusting the apodization to the imaging depth. However, such an adjustment is out of the scope of this paper. Therefore, for simplicity, we do not introduce dynamic apodization in further experiments.

C. Results Using FoCUS

We next compare the performance of FoCUS in axial and lateral dimensions to that of precompression and postcompression techniques. Theoretically, FoCUS is equivalent to beamforming precompression since it performs the same processing in the dual frequency domain. The differences, however, stem from the approximation in (23), namely, from the fact that only N_q Fourier coefficients of the distortion function defined in (18) are used. As we see next, the experiments show that the approximation only affects the performance in lateral direction.

1) Performance in Axial Dimension: Fig. 8(a) and (b) presents scan-lines of a point scatterer located at 10 and 80 mm from the transducer, respectively. As can be seen, the axial PSFs of FoCUS and beamforming precompression are identical in terms of main lobe width, and their sidelobes are extremely close at both depths. This implies that FoCUS preserves the performance in terms of contrast and resolution in the axial dimension. The above results are obtained for $N_q = 9$, however, even coarser approximation corresponding to lower values of N_q has almost no effect on the axial dimension. This implies that the approximation in (23) has almost no effect on the performance in the axial dimension. For $N_q = 3$, the same main lobe width is obtained with only 1.3-dB degradation in sidelobes level. This is significantly lower than the 9-dB degradation of beamforimg postcompression.

The difference in the axial performance can be easily seen in the resulting images. Fig. 5(a) and (b) shows beamforming precompression and postcompression. FoCUS with $N_q = 29$ and $N_q = 9$ are presented in Fig. 9(a) and (b), respectively. A zoomed-in view on the first three scatterers, presented in Fig. 6, verifies that the axial resolution of FoCUS with both $N_q = 29$ and $N_q = 9$ is the same as beamforming precompression. In fact, it can be observed that Fig. 5(a) and (d) looks the same, implying that FoCUS achieves the same image quality as beamforming precompression which is optimal for coded imaging. Figs. 5 and 6 demonstrate that in terms of axial resolution FoCUS outperforms beamforming postcompression for shallow depths. The performance in lateral direction is discussed next.

2) Performance in Lateral Dimension: As mentioned in Section IV, the number of Q-coefficients controls the quality of the approximation in (21). The results presented above show that this approximation affects mostly the performance in the lateral dimension.

To study the effect of the approximation level on the lateral resolution, we measure the main lobe width of the lateral PSF

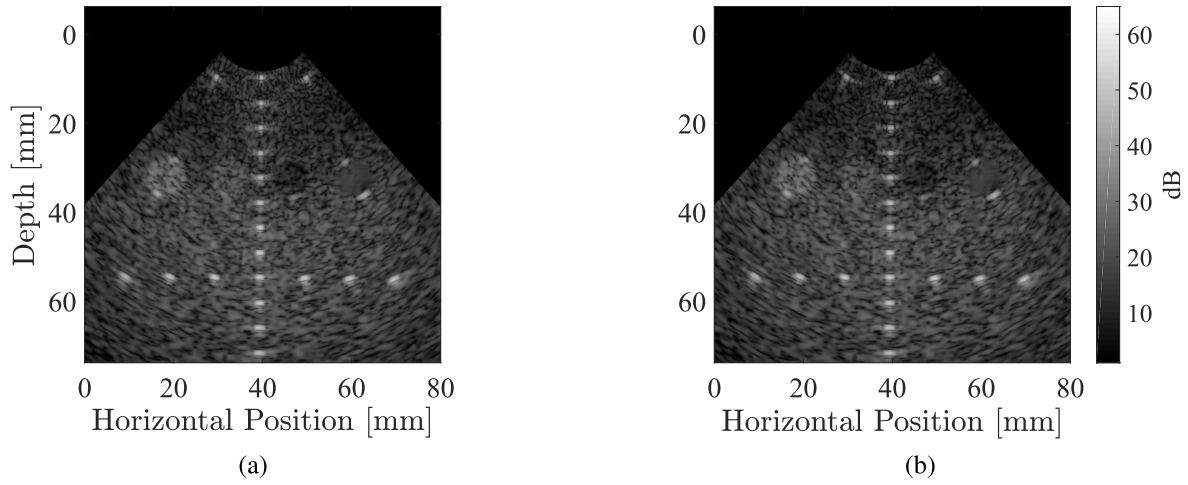

Fig. 9. Experimental results. Phantom scans obtained by (a) FDBF with $N_q = 29$ and (b) FDBF with $N_q = 9$.

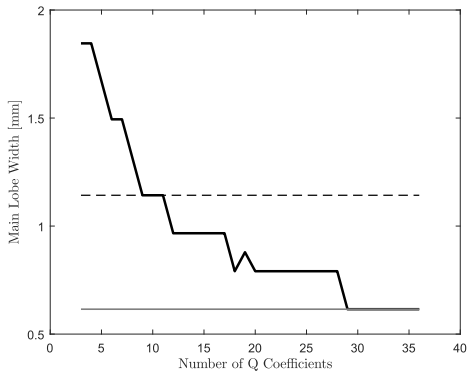

Fig. 10. Main lobe width of the lateral PSF measured for a scatterer at 10-mm depth, as a function of N_q. Main lobe widths obtained with beamforming precompression and postcompression are plotted in gray thin line and dashed line, respectively.

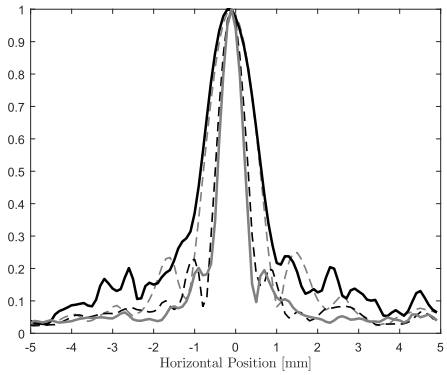

Fig. 11. Lateral PSF measured for a scatterer at 10 mm. PSF corresponding to beamforming precompression and postcompression are plotted in gray solid and black lines, respectively. Black dashed and gray lines correspond to frequency domain processing with $N_q = 29$ and 9, respectively.

corresponding to the scatterer located at 10 mm from the transducer. We compare it to beamforming postcompression and precompression. Fig. 10 presents the main lobe width as a function of N_q. As expected, the lateral resolution decreases with N_q. For $N_q \geq 29$, FoCUS obtains the same lateral resolution as beamforming precompression, and it outperforms beamforming postcompression as long as $N_q \geq 9$. To verify the performance in terms of lateral sidelobes, we compare the lateral PSF obtained by beamforming precompression and postcompression with those obtained by FoCUS with $N_q = 29$ and 9. The results are shown in Fig. 11. As can be seen, both the main lobe width and the sidelobes level are comparable for beamforming precompression and FoCUS with $N_q = 29$. For $N_q = 9$, the main lobe width of FoCUS is similar to beamforming postcompression, while the distant sidelobes are higher for beamforming postcompression.

To quantitatively evaluate FoCUS, we computed an error between the precompression and FoCUS for $N_q = 9$ and 29 similar to the definition in (26). This allows to assess the overall effect of both the main-lobe width and the sidelobes as a function of depth. As can be seen in Fig. 7, FoCUS outperforms beamforming postcompression for most imaging depths for both $N_q = 29$ and $N_q = 9$.

Our results demonstrate that the proposed method obtains high image quality, and for N_q large enough it yields the performance of beamforming precompression both in lateral and axial dimensions. The number of Q-coefficients, N_q, defines the reduction in computational complexity which is discussed next.

D. Computational Complexity

We analyze the computational complexity of beamforming precompression and postcompression and FoCUS while considering only multiplications. The number of samples comprising each scan-line is denoted by N_s, and is determined by the sampling rate and imaging depth. According to (25), the number of multiplications needed for a computation of one scan-line using K coefficients from the set $\{c_{\mathrm{CE}}[k]\}$ is

$$N_F = MKN_q + \frac{N_s}{2}\log N_s \tag{27}$$

including the inverse Fourier transform. Here M is the number of transducer elements and N_q denotes the number of $\tilde{Q}_{k,m;\theta}[n]$ coefficients taken for the approximation in (25).

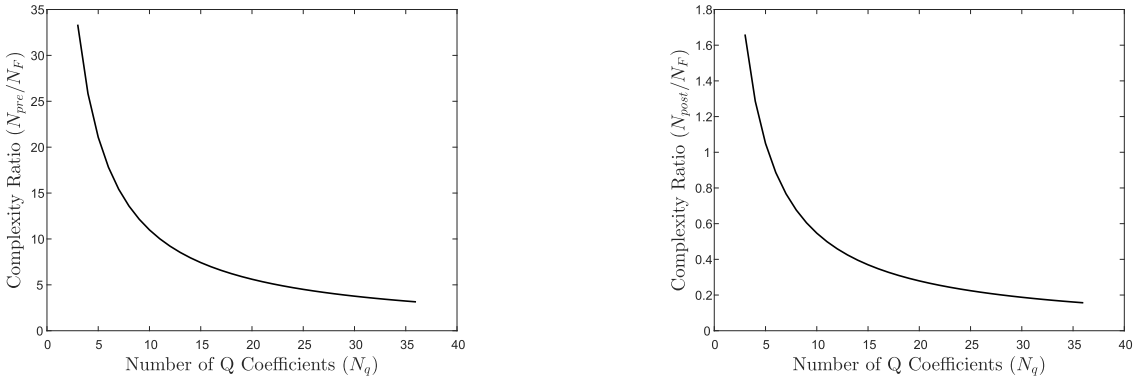

Fig. 12. Computational complexity ratio between FoCUS and (a) precompression and (b) postcompression.

When applying conventional beamforming precompression, the computation includes the complexity of M MFs and interpolation of M signals to apply the time-varying delays. Assuming that the values of the detected signal $\varphi_m(t)$ at $\tau_m(t;\theta)$ are obtained by linear interpolation with linear complexity and an efficient MF implementation using FFT

$$N_{\text{pre}} = MN_s + M\left(\frac{3(N_s+N_h)}{2}\log(N_s+N_h) + N_s + N_h\right) \tag{28}$$

multiplications are needed.

The computational complexity of beamforming postcompression includes interpolation of M signals as in beamforming precompression, while the MF is applied only once on the beamformer output. This is the major savings of the postcompression method at the expense of compression performance. Compression is performed on baseband beamformed data obtained by demodulation and decimation of the beamformer output as proposed in [21] and [22]. To the best of our knowledge this is the most efficient implementation of beamforming postcompression. As shown in [21] and [22], the implementation of matched filtering using baseband data does not lead to further reduction of compression performance. The overall computational complexity of this method is

$$N_{\text{post}} = MN_s + \frac{3(\tilde{N_s}+\tilde{N_h})}{2}\log(\tilde{N_s}+\tilde{N_h}) + \tilde{N_s} + \tilde{N_h} \tag{29}$$

where

$$\tilde{N_s} = N_s/P, \quad \tilde{N_h} = N_h/P. \tag{30}$$

Here P stands for the decimation factor which is equal to the oversampling factor, namely, $P = f_s/f_0$.

For a sampling rate of $f_s = 4f_c$ the MF length is $N_h = 274$ and $N_s = 1392$. Using a linear FM with time-bandwidth product $D = 60$ and the above sampling rate, the bandwidth of the beamformed signal contains $K = 260$ Fourier coefficients. Table I summarizes these parameters.

Fig. 12(a) shows the computational complexity ratio between beamforming precompression and FoCUS as a function of N_q. For $N_q = 29$ our method achieves 4-fold complexity reduction while yielding optimal axial and lateral resolution. When choosing lower values of N_q further complexity reduction is achieved yielding up to 33-fold reduction for $N_q = 3$. The lateral resolution is degraded accordingly as shown in Fig. 10, while the axial resolution is preserved.

TABLE I
SYSTEM PARAMETERS

Parameter	Description	Value
f_c	Transducer central frequency [MHz]	2.9
f_s	Sampling frequency	$4f_c$
N_s	Samples per element	1392
N_h	Matched filter length	274
K	Number of $c_{CE}[k]$ coefficients	260

Comparing the complexity of FoCUS to that of beamforming postcompression, it can be seen in Fig. 12(b), that the proposed method outperforms postcompression for $N_q \leq 5$. We note that N_s and N_h depend on the oversampling factor, P, and are given by

$$N_s = TPf_c, \quad N_h = DP. \tag{31}$$

Thus, N_{pre}/N_F as well as N_{post}/N_F increases with P, meaning that the savings in computational load is more significant for higher oversampling factors. For example, taking $P = 10$ leads to 11-fold reduction for $N_q = 29$ and 77-fold reduction for $N_q = 3$ when comparing FoCUS and precompression. In addition, for $P = 10$ the proposed method outperforms postcompression for $N_q \leq 12$.

VI. CONCLUSION

In this paper, we present a method allowing to reduce the computational load required by CE array imaging. The proposed approach is based on integration of pulse compression of each one of the detected signals to computationally efficient frequency domain processing. FDBF computes the Fourier coefficients of the beam as a weighted average of those of the detected signals. We show that in frequency, pulse compression of each channel can be performed together with beamforming by appropriate modification of the weights required for FDBF. As a result, matched filtering is applied at each detected signal without additional computational cost to the FDBF technique. Our method enables efficient implementation of CE, making it a feasible approach in array imaging with the potential to enhance SNR as well as improve imaging depth and frame rate.

The reduction in computational complexity achieved by FoCUS is a function of the number of Fourier coefficients N_q. Coarse approximation, namely, small values of N_q, affect the performance of FoCUS. It was shown experimentally that only lateral resolution is decreased in this case, while the performance in axial dimension is insensitive to the reduction of N_q.

The proposed method, FoCUS, was verified on experimental data acquired by a Verasonics system with a 64-element probe. We compared our results with beamforming precompression, which is the optimal implementation for CE array imaging. We evaluated the reduction in computational load for different oversampling factors P. It was shown that for $P = 4$ and $P = 10$ FoCUS achieves the same image quality with 4- and 11-fold reduction in computational complexity, respectively. Further reduction, up to 33-fold for $P = 4$ and up to 77-fold for $P = 10$, can be obtained at the expense of decreased lateral resolution. As a result our method enables adjusting lateral resolution to available computational power. It is important to mention that FoCUS preserves optimal axial resolution regardless of the reduction in complexity. This is in contrast to beamforming postcompression, commonly used to reduce the computational load. For low values of N_q FoCUS outperforms the most efficient implementation of beamforming postcompression and preserves optimal axial resolution. It is important to keep in mind, however, that lateral resolution obtained by FoCUS in this case may be degraded compared to postcompression. This should be taken into account when defining the optimal processing strategy.

Parallelization may significantly speed up the beamforming precompression where each detected signal is compressed independently of the others. This holds for FoCUS as well where each $\hat{c}_m^{\mathrm{CE}}[k]$ of (24) can be computed in parallel.

The performance in terms of lateral resolution may be potentially improved by postprocessing coherence-based techniques [37], [38]. The above methods are applied on beamformed data and result in up to twofold improvement of the lateral resolution. Implementing these methods directly in frequency and integrating them with FoCUS may alow to obtain maximal complexity reduction without compromising lateral resolution.

REFERENCES

[1] C. E. Cooke, "The early history of pulse compression radar-the history of pulse compression at Sperry Gyroscope Company," *IEEE Trans. Aerosp. Electron. Syst.*, vol. 24, no. 6, pp. 825–833, Nov. 1988.

[2] A. W. Rihaczek, *Principles of High-Resolution Radar*. New York, NY, USA: McGraw-Hill, 1969.

[3] R. Y. Chiao and X. Hao, "Coded excitation for diagnostic ultrasound: A system developer's perspective," *IEEE Trans. Ultrason., Ferroelect., Freq. Control*, vol. 2, no. 52, pp. 160–170, Feb. 2005.

[4] T. Misaridis and J. A. Jensen, "Use of modulated excitation signals in medical ultrasound. Part II: Design and performance for medical imaging applications," *IEEE Trans. Ultrason., Ferroelect., Freq. Control*, vol. 52, no. 2, pp. 192–207, Feb. 2005.

[5] M. O'Donnell, "Coded excitation system for improving the penetration of real-time phased-array imaging systems," *IEEE Trans. Ultrason., Ferroelect., Freq. Control*, vol. 39, no. 3, pp. 341–351, May 1992.

[6] M. L. Oelze, "Bandwidth and resolution enhancement through pulse compression," *IEEE Trans. Ultrason., Ferroelect., Freq. Control*, vol. 54, no. 4, pp. 768–781, Apr. 2007.

[7] A. Polpetta and P. Banelli, "Design and performance of huffman sequences in medical ultrasound coded excitation," *IEEE Trans. Ultrason., Ferroelect., Freq. Control*, vol. 59, no. 4, pp. 630–647, Apr. 2012.

[8] J. K. Tsou, J. Liu, and M. F. Insana, "Modeling and phantom studies of ultrasonic wall shear rate measurements using coded pulse excitation," *IEEE Trans. Ultrason., Ferroelect., Freq. Control*, vol. 53, no. 4, pp. 724–734, Apr. 2006.

[9] J. Cowe, J. Gittins, and D. H. Evans, "Improving performance of pulse compression in a Doppler ultrasound system using amplitude modulated chirps and Wiener filtering," *Ultrasound Med. Biol.*, vol. 34, no. 2, pp. 326–333, Feb. 2008.

[10] A. Ramalli, E. Boni, A. Dallai, F. Guidi, S. Ricci, and P. Tortoli, "Coded spectral Doppler imaging: From simulation to real-time processing," *IEEE Trans. Ultrason., Ferroelect., Freq. Control*, vol. 63, no. 11, pp. 1815–1824, Nov. 2016.

[11] D. J. Muzilla, R. Y. Chiao, and A. L. Hall, "Method and apparatus for color flow imaging using coded excitation with single codes," U.S. Patent 5 938 611, Aug. 17, 1999.

[12] J. Liu and M. F. Insana, "Coded pulse excitation for ultrasonic strain imaging," *IEEE Trans. Ultrason., Ferroelect., Freq. Control*, vol. 52, no. 2, pp. 231–240, Feb. 2005.

[13] M. Vogt and H. Ermert, "Development and evaluation of a high-frequency ultrasound-based system for *in vivo* strain imaging of the skin," *IEEE Trans. Ultrason., Ferroelect., Freq. Control*, vol. 52, no. 3, pp. 375–385, Mar. 2005.

[14] A. Novell, S. V. D. Meer, M. Versluis, N. D. Jong, and A. Bouakaz, "Contrast agent response to chirp reversal: Simulations, optical observations, and acoustical verification," *IEEE Trans. Ultrason., Ferroelect., Freq. Control*, vol. 56, no. 6, pp. 1199–1206, Jun. 2009.

[15] K. L. Gammelmark and J. A. Jensen, "Multielement synthetic transmit aperture imaging using temporal encoding," *IEEE Trans. Med. Imag.*, vol. 22, no. 4, pp. 552–563, Apr. 2003.

[16] M. O'Donnell and Y. Wang, "Coded excitation for synthetic aperture ultrasound imaging," *IEEE Trans. Ultrason., Ferroelect., Freq. Control*, vol. 52, no. 2, pp. 171–176, Feb. 2005.

[17] P. Song, M. W. Urban, A. Manduca, J. F. Greenleaf, and S. Chen, "Coded excitation plane wave imaging for shear wave motion detection," *IEEE Trans. Ultrason., Ferroelect., Freq. Control*, vol. 62, no. 7, pp. 1356–1372, Jul. 2015.

[18] M. Lewandowski and A. Nowicki, "High frequency coded imaging system with RF software signal processing," *IEEE Trans. Ultrason., Ferroelect., Freq. Control*, vol. 55, no. 8, pp. 1878–1882, Aug. 2008.

[19] T. Misaridis and J. A. Jensen, "Use of modulated excitation signals in medical ultrasound. Part III: High frame rate imaging," *IEEE Trans. Ultrason., Ferroelect., Freq. Control*, vol. 52, no. 2, pp. 208–219, Feb. 2005.

[20] R. Bjerngaard and J. A. Jensen, "Should compression of coded waveforms be done before or after focusing?" *Proc. SPIE*, vol. 4687, pp. 47–58, Apr. 2002.

[21] C. Yoon, W. Lee, J. H. Chang, T.-K. Song, and Y. Yoo, "An efficient pulse compression method of chirp-coded excitation in medical ultrasound imaging," *IEEE Trans. Ultrason., Ferroelect., Freq. Control*, vol. 60, no. 10, pp. 2225–2229, Oct. 2013.

[22] A. Ramalli, F. Guidi, E. Boni, and P. Tortoli, "A real-time chirp-coded imaging system with tissue attenuation compensation," *Ultrasonics*, vol. 60, pp. 65–75, Jul. 2015.

[23] B. D. Steinberg, "Digital beamforming in ultrasound," *IEEE Trans. Ultrason., Ferroelect., Freq. Control*, vol. 39, no. 6, pp. 716–721, Nov. 1992.

[24] N. Wagner, Y. C. Eldar, and Z. Friedman, "Compressed beamforming in ultrasound imaging," *IEEE Trans. Signal Process.*, vol. 60, no. 9, pp. 4643–4657, Sep. 2012.

[25] T. Chernyakova and Y. C. Eldar, "Fourier-domain beamforming: The path to compressed ultrasound imaging," *IEEE Trans. Ultrason., Ferroelect., Freq. Control*, vol. 61, no. 8, pp. 1252–1267, Aug. 2014.

[26] A. Burshtein, M. Birk, T. Chernyakova, A. Eilam, A. Kempinski, and Y. C. Eldar, "Sub-Nyquist sampling and fourier domain beamforming in volumetric ultrasound imaging," *IEEE Trans. Ultrason., Ferroelect., Freq. Control*, vol. 63, no. 5, pp. 703–716, May 2016.

[27] Y. C. Eldar, *Sampling Theory: Beyond Bandlimited Systems*. Cambridge, U.K.: Cambridge Univ. Press, 2015.

[28] T. Misaridis and J. A. Jensen, "Use of modulated excitation signals in medical ultrasound. Part I: Basic concepts and expected benefits," *IEEE Trans. Ultrason., Ferroelect., Freq. Control*, vol. 52, no. 2, pp. 177–191, Feb. 2005.

[29] D. R. Wehner, *High Resolution Radar*, 2nd ed. Norwood, MA, USA: Artech House, 1995.
[30] J. A. Jensen, *Estimation of Blood Velocities Using Ultrasound: A Signal Processing Approach*. Cambridge, U.K.: Cambridge Univ. Press, 1996.
[31] C. Cook and M. Bernfeld, *Radar Signals: An Introduction to Theory and Application*. Boca Raton, FL, USA: Academic, 1967.
[32] H. L. Van Trees, *Optimum Array Processing: Part IV of Detection, Estimation, and Modulation Theory*. Hoboken, NJ, USA: Wiley, 2004.
[33] R. Cohen, Y. Sde-Chen, T. Chernyakova, C. Fraschini, J. Bercoff, and Y. C. Eldar, "Fourier domain beamforming for coherent plane-wave compounding," in *Proc. IEEE Int. Ultrason. Symp. (IUS)*, Oct. 2015, pp. 1–4.
[34] J. R. Williams, "Fast beam-forming algorithm," *J. Acoust. Soc. Amer.*, vol. 44, no. 5, p. 1454, 1968.
[35] P. Rudnick, "Digital beamforming in the frequency domain," *J. Acoust. Soc. Amer.*, vol. 46, no. 5A, p. 1089, 1969.
[36] M. Tanter and M. Fink, "Ultrafast imaging in biomedical ultrasound," *IEEE Trans. Ultrason., Ferroelect., Freq. Control*, vol. 61, no. 1, pp. 102–119, Jan. 2014.
[37] J. Camacho, M. Parrilla, and C. Fritsch, "Phase coherence imaging," *IEEE Trans. Ultrason., Ferroelect., Freq. Control*, vol. 56, no. 5, pp. 958–974, May 2009.
[38] P.-C. Li and M.-L. Li, "Adaptive imaging using the generalized coherence factor," *IEEE Trans. Ultrason., Ferroelect., Freq. Control*, vol. 50, no. 2, pp. 128–141, Feb. 2003.

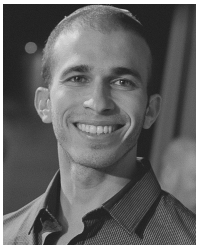

Almog Lahav received the B.Sc. degree (*cum laude*) in electrical engineering from the Technion–Israel Institute of Technology, Haifa, Israel, in 2015, where he is currently pursuing the M.Sc. degree in electrical engineering.

From 2013 to 2015, he was with Intel Corporation, where he was involved in design and implementation of signal processing systems. Since 2015, he has been a Teaching Assistant with the Viterbi Faculty of Electrical Engineering, Technion–Israel Institute of Technology. His research interests include signal processing, medical imaging, manifold learning, and geometric methods for data analysis.

Tanya Chernyakova (S'13) received the B.Sc. degree (*cum laude*) in biomedical engineering from the Technion–Israel Institute of Technology, Haifa, Israel, in 2011, where she is currently pursuing the Ph.D. degree in electrical engineering.

Her research interests include theoretical aspects of signal processing, sampling theory, compressed sensing, medical imaging, array signal processing, and advanced signal processing methods for ultrasonic imaging.

Yonina C. Eldar (S'97–M'02–SM'07–F'13) is a Professor with the Department of Electrical Engineering, Technion–Israel Institute of Technology, Haifa, Israel, where she holds the Edwards Chair in Engineering. She is also an Adjunct Professor with Duke University, Durham, NC, USA, and a Research Affiliate with the Research Laboratory of Electronics, Massachusetts Institute of Technology, Cambridge, MA, USA. She was a Visiting Professor at Stanford University, Stanford, CA, USA.

Prof. Eldar is a member of the Israel Academy of Sciences and Humanities and a EURASIP Fellow. She has received many awards for excellence in research and teaching, including the IEEE Signal Processing Society Technical Achievement Award, the IEEE/AESS Fred Nathanson Memorial Radar Award, the IEEE Kiyo Tomiyasu Award, the Michael Bruno Memorial Award from the Rothschild Foundation, the Weizmann Prize for Exact Sciences, and the Wolf Foundation Krill Prize for Excellence in Scientific Research. She is the Editor-in-Chief of *Foundations and Trends in Signal Processing*, and serves the IEEE on several technical and award committees.